

Angle dependent magnetoresistance measurements in $\text{Tl}_2\text{Ba}_2\text{CuO}_{6+\delta}$ and the need for anisotropic scattering

J. G. Analytis, M. Abdel-Jawad, L. Balicas[†], M. M. J. French and N. E. Hussey
H. H. Wills Physics Laboratory, University of Bristol, Tyndall Avenue, Bristol, BS8 1TL, UK and
[†]*National High Magnetic Field Laboratory, Florida State University, Tallahassee, FL-32306, USA*

The angle-dependent interlayer magnetoresistance of overdoped $\text{Tl}_2\text{Ba}_2\text{CuO}_{6+\delta}$ has been measured in high magnetic fields up to 45 Tesla. A conventional Boltzmann transport analysis with no basal-plane anisotropy in the cyclotron frequency ω_c or transport lifetime τ is shown to be inadequate for explaining the data. We describe in detail how the analysis can be modified to incorporate in-plane anisotropy in these two key quantities and extract the degree of anisotropy for each by assuming a simple four-fold symmetry. While anisotropy in ω_c and other Fermi surface parameters may improve the fit, we demonstrate that the most important anisotropy is that in the transport lifetime, thus confirming its role in the physics of overdoped superconducting cuprates.

PACS numbers: 74.72.Jt, 71.18.+y, 72.10.Bg, 73.43.Qt

I. INTRODUCTION

There are many routes to investigating the mechanism of high-temperature superconductivity and naively one might expect the normal state to be the simplest. Despite concerted experimental effort however,¹ the normal state properties of cuprates remain a profound theoretical challenge.² Indeed, even from the earliest transport measurements in these compounds it was clear that the normal state was far from conventional.³ Arguably the most remarkable phenomena are the distinct power laws of the in-plane resistivity ρ_{ab} and inverse Hall angle $\cot\Theta_H$ temperature dependences. In optimally doped $\text{YBa}_2\text{Cu}_3\text{O}_{7-\delta}$ (YBCO) and $\text{La}_{2-x}\text{Sr}_x\text{CuO}_4$ (LSCO) for example, $\rho_{ab}(T)$ varies linearly with temperature over a wide temperature range, whereas $\cot\Theta_H$ maintains a strong T^2 dependence.^{4,5} In other words, it is as if these materials exhibit distinct scattering mechanisms which are separately manifested according to the experimental probe being considered. Anderson coined the phrase ‘lifetime separation’ to describe this anomalous behavior and today its interpretation remains one of the greatest obstacles to the development of a coherent description of the normal state quasiparticle dynamics in high- T_c cuprates.

Three contrasting approaches dominate the current thinking on the transport problem in cuprates; Anderson’s two-lifetime picture,⁶ marginal Fermi-liquid (MFL) phenomenology⁷ and models based on fermionic quasiparticles that invoke specific (anisotropic) scattering mechanisms within the basal plane.^{8–12} In the two-lifetime approach, scattering processes involving momentum transfer perpendicular and parallel to the Fermi surface are governed by independent transport and Hall scattering rates $1/\tau_{tr}$ and $1/\tau_H$ with different T -dependencies. The proponents of the MFL hypothesis assume a single T -linear scattering rate which naturally accounts for $\rho_{ab}(T)$, but introduce an unconventional expansion in the magnetotransport response whereby the Hall angle, for example, is given by the square of the transport lifetime.¹³ This anomalous expansion is at-

tributed to anisotropy in the (elastic) impurity scattering rate, possibly due to small-angle scattering off impurities located away from the CuO_2 plane.¹³

Attempts to explain the anomalous behavior of $\rho_{ab}(T)$ and $\cot\Theta_H(T)$ in cuprates within a Fermi-liquid (FL) approach have centered around the assumption of a (single) *inelastic* scattering rate that is strongly dependent on the quasiparticle wave-number \mathbf{k} . This anisotropy can arise either due to anisotropic electron-electron (possibly Umklapp) scattering¹² or coupling to a singular bosonic mode, be that of spin,^{8,9} charge¹⁰ or d -wave superconducting fluctuations.¹¹ Generating a clear separation of lifetimes within these single-lifetime scenarios however requires a subtle balancing act between different regions in \mathbf{k} -space with distinct T -dependencies.¹⁴

In order to test these various proposals and to proceed towards a theoretical consensus, information on the momentum (\mathbf{k}) and energy (ω or T) dependence of the transport lifetime τ at or near the Fermi level ϵ_F is urgently required. This is a non-trivial exercise however since the transport coefficients themselves are angle-averaged quantities involving differently weighted integrations around the Fermi surface (FS). Whilst angle resolved photoemission spectroscopy (ARPES) can probe directly the in-plane quasi-particle lifetime via the imaginary part of the self-energy $\text{Im}\Sigma(\mathbf{k},\omega)$, its relevance to DC transport is still unclear.¹⁵ Moreover, there remains some dispute as to the correct form of $\text{Im}\Sigma(\mathbf{k},\omega)$ even for samples with nominally the same composition.^{16,17}

Measurements of interlayer magnetoresistance as a function of angle have yielded important information about the FS topology (size and shape) in a variety of layered metals including organic conductors¹⁸ and quasi-two-dimensional (q2D) oxides.^{19–21} In a recent paper, we showed that this technique could be developed to extract information on the scattering rate anisotropy and applied the technique to overdoped $\text{Tl}_2\text{Ba}_2\text{CuO}_{6+\delta}$ (Tl2201).²² In the present paper, we present a more thorough and detailed analysis of our angle-dependent magnetoresistance (ADMR) measurements on overdoped Tl2201, focusing

in particular on the procedure used to fit ADMR and show how this analysis fails at higher temperatures unless one includes such anisotropy in τ . We progressively introduce anisotropy into the formalism, and explore the effects of this both in the cyclotron frequency ω_c and the transport lifetime τ . The approach presented here is similar to that described recently by Kennett and McKenzie who derived a generalized expression for ADMR in layered metals with basal-plane anisotropy.²³ In this paper, we focus on issues pertinent to Tl2201, the importance of each parameter in fitting the ADMR signal and their interdependence, and the issue of sample misalignment. Although it is difficult to isolate anisotropy in one from anisotropy in the other, the strong temperature evolution of the ADMR signal (and subsequent measurements of its doping dependence¹⁵) suggests that the dominant anisotropy is in τ and not ω_c . The paper is set out as follows. Section II describes the FS parameterization of Tl2201 and the necessary symmetry considerations with respect to the ADMR analysis. Section III briefly describes the ADMR experiment itself. The Boltzmann formalism and the resulting analysis is described in Section IV for the cases where the parameters ω_c and τ are both isotropic and anisotropic (within the basal-plane). Our conclusions are presented in Section V.

II. THE THREE-DIMENSIONAL FERMI SURFACE OF $\text{Tl}_2\text{Ba}_2\text{CuO}_{6+\delta}$

The present FS parameterization is identical to that used previously^{20,22,23} and so shall be described here only briefly. The interested reader is referred to [Ref.19] which details a similar parameterization of the α sheet of Sr_2RuO_4 . Being extended in the k_z direction, the quasiparticle dispersion contains a finite (though small \sim meV) transfer integral $t_\perp(\phi, k_z)$, where ϕ is the azimuthal angle in the $k_x - k_y$ plane. The parameter $t_\perp(\phi, k_z)$ is anisotropic in the plane and the Fermi wave-vector k_F is therefore modulated by both the in-plane dispersion and by $t_\perp(\phi, k_z)$. The clearest way to express this is by expanding k_F into cylindrical harmonics^{19,20}

$$k_F(\phi, \kappa) = \sum_{m,n=0} k_{mn} \begin{Bmatrix} c \\ s \end{Bmatrix} \begin{Bmatrix} c \\ s \end{Bmatrix} \begin{Bmatrix} \cos \\ \sin \end{Bmatrix} n\kappa \times \begin{Bmatrix} \cos \\ \sin \end{Bmatrix} m\phi. \quad (1)$$

where $\{c\}$ denote coefficients corresponding to cosine and sine terms, $\kappa = k_z c/2$ and $c = 23.2\text{\AA}$ is the inter-layer dimension of the unit cell. The symmetry of the Brillouin zone limits the number of parameters of interest and a pictorial illustration of this is shown in Figure 1. In the k_z direction, inversion symmetry $\kappa \rightarrow -\kappa$ requires that the only terms containing κ are cosines. Three further symmetries restrict the parameterization: (i) the two-fold rotational symmetry $\phi \rightarrow \phi + \pi$, (ii) the mirror plane $\phi \rightarrow -\pi/2 - \phi$ and (iii) the screw symmetry $\kappa, \phi \rightarrow$

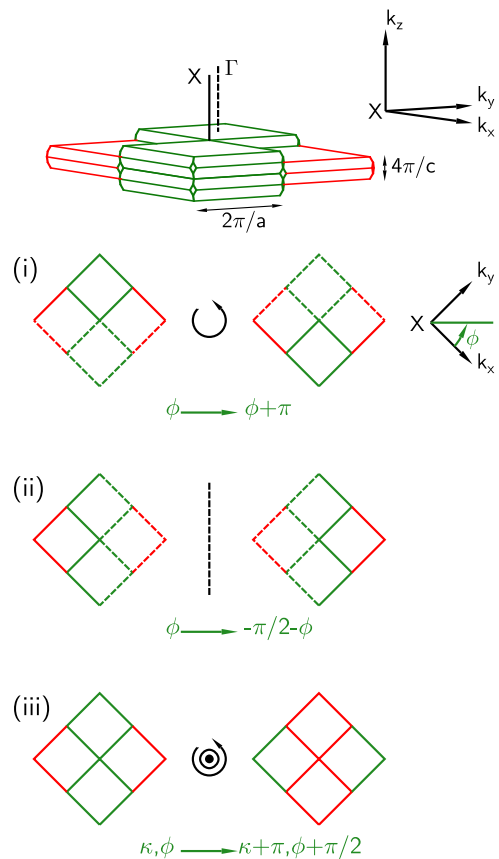


FIG. 1: (Color online) The Brillouin zone stacking for $\text{Tl}_2\text{Ba}_2\text{CuO}_{6+\delta}$. There is inversion symmetry about the $k_x - k_y$ plane: $\kappa, \phi \rightarrow -\kappa, \phi$ and three further symmetries about the axis along the X -line. As described in the text they are (i) the two fold symmetry $\phi \rightarrow \phi + \pi$, (ii) the mirror symmetry $\phi \rightarrow -\pi/2 - \phi$ and finally (iii) the screw symmetry involving a translation in the k_z direction and a rotation: $\kappa, \phi \rightarrow \kappa + \pi, \phi + \pi/2$.

$\kappa + \pi, \phi + \pi/2$. The transformations differ from those in Ref.19 because of a different choice in coordinate axes, but the operations are identical. The first symmetry requires that all m be even. The next symmetry requires that all cosine terms have $m \bmod 4 \equiv 0$ and all sine terms have $m \bmod 4 \equiv 2$. For example, $\cos 4\phi = \cos 4(-\pi/2 - \phi)$ whereas $\cos 2\phi = -\cos 2(-\pi/2 - \phi)$. The reverse is true for the sine terms. The final symmetry requires that all of the cosine terms be accompanied by n that are even and the sine terms be accompanied by any n that are odd. For example, $\cos \kappa \sin 2\phi = \cos(\kappa + \pi) \sin 2(\pi/2 + \phi)$, but $\cos 2\kappa \sin 2\phi = -\cos 2(\kappa + \pi) \sin 2(\pi/2 + \phi)$. The converse is of course true for the cosine terms that have $m \bmod 4 \equiv 0$. Eq. 1 can thus be simplified to

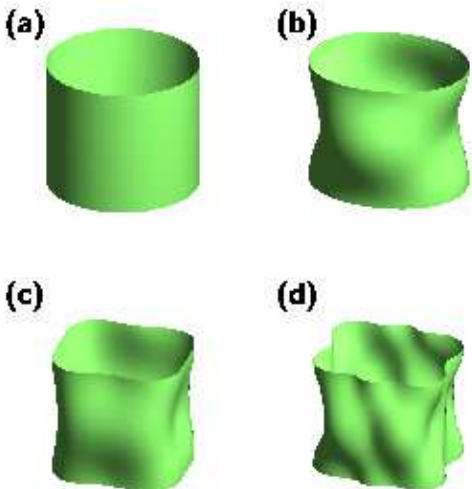


FIG. 2: (Color online) Quasi-2D Fermi surfaces described by Eq. 2 with progressive inclusion of cylindrical harmonics (a) k_{00} , (b) k_{21} , (c) k_{04} and (d) k_{61} and k_{101} .

$$k_F(\phi, \kappa) = \sum_{\substack{m, n = 0 \\ m \bmod 4 = 0 \\ n \text{ even}}} k_{mn} \cos(n\kappa) \cos(m\phi) + \sum_{\substack{m, n = 0 \\ m \bmod 4 = 2 \\ n \text{ odd}}} k_{mn} \cos(n\kappa) \sin(m\phi). \quad (2)$$

We have shown previously that the minimum number of parameters required to fit the data that simultaneously satisfy these symmetry constraints are k_{00} , k_{04} , k_{21} , k_{61} and k_{101} .²⁰ Figure 2 shows the warping created by progressive inclusion of these parameters, beginning with a dispersionless ($t_{\perp} = 0$) isotropic FS. Eq. 2 has exact four-fold symmetry though the modulation t_{\perp} gives rise to eight highly symmetric points where the transfer integral vanishes, as predicted by band-structure calculations.²⁴ Figure 3 shows the projection of the three-dimensional FS as deduced by ADMR²⁰ overlaid on that determined by ARPES²⁵ (see Eq. 15; this curve corresponds to the nominal doping level of this crystal). The agreement is very good, but most importantly the two experiments, to a good approximation, share the eight points of high symmetry. For ease of computation, the Fermi surface can be described by

$$\epsilon_F(\kappa, \phi) = \frac{\hbar^2}{2m} k_F^{\parallel 2}(\phi) - 2t_{\perp} \cos \kappa \times \frac{a}{\pi} (k_{21} \sin 2\phi + k_{61} \sin 6\phi + k_{101} \sin 10\phi), \quad (3)$$

where $k_F^{\parallel}(\phi) = k_{00} + k_{04} \cos(4\phi)$ and $a = 3.866 \text{ \AA}$ is the in-plane lattice parameter.

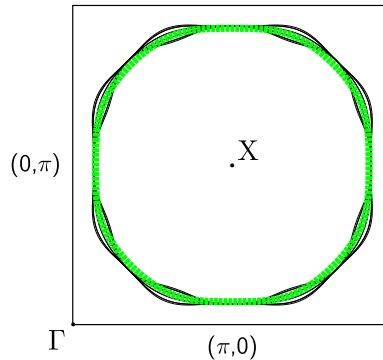


FIG. 3: (Color online) The projection of the 3D dispersion for overdoped Tl2201 as determined by ADMR (thin black lines), plotted over the ARPES (thick green line) results for a compound with a nominally similar doping.²⁵ The warping of the transfer integral is exaggerated by approximately 100 times for clarity.

III. EXPERIMENTAL

Tl2201 is the most suitable cuprate system for ADMR studies due to its single Fermi sheet,²⁶ its strong two-dimensionality,²⁷ its low residual resistivity^{28–30} and accessibility to the whole overdoped region of the cuprate phase diagram.³¹ Single crystals were fabricated using a self-flux method in alumina crucibles.³² As-grown crystals are naturally overdoped and the doping level (and therefore the desired T_c) is set by annealing in oxygen, argon or in vacuum.³² The crystal used in this study ($300 \mu\text{m} \times 150 \mu\text{m} \times 20 \mu\text{m}$) was annealed in oxygen at 600K for 200min resulting in $T_c \approx 17\text{K}$. Electrical contacts were attached using Dupont 6838 silver paste in a quasi-Montgomery 4-wire configuration. ADMR measurements were performed at 45T in the hybrid magnet at the National High Magnetic Field Laboratory, Tallahassee, Florida using a probe with a two-axis rotator. Initially, the platform on which the sample was mounted was rotated by an azimuthal angle ϕ_{exp} and then the interplane resistivity ρ_{zz} was measured as the polar angle θ_{exp} was swept at constant temperature and constant field (see Figure 4).

IV. FITTING OF THE ANGLE-DEPENDENT MAGNETORESISTANCE IN TL2201

In this section we review how the Boltzmann transport equation can be used to fit the ADMR data. We begin with the simplest case whereby both ω_c and τ are isotropic before going on to discuss the more general case in which both parameters are anisotropic within the conducting plane.

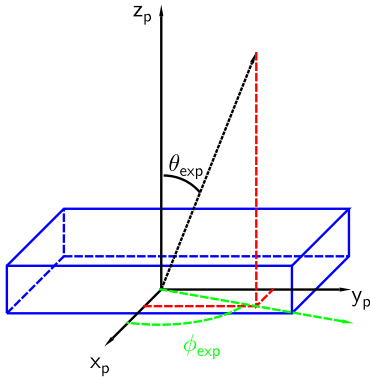


FIG. 4: (Color online) Diagram describing the ADMR experimental technique, whereby the sample (schematically shown in blue) is rotated by an azimuthal angle ϕ_{exp} with respect to the laboratory frame (x_p, y_p, z_p) , and then data are continuously taken as a function of polar angle θ_{exp} . In the actual experiment, the crystallographic (x_c, y_c) plane does not lie exactly in the laboratory frame due to a slight misalignment and the corresponding polar angle $\theta_{\text{crys}} \equiv \theta$ (taken as the angle between the field direction and the normal to the plane on the sample) differs from θ_{exp} . Moreover, the azimuthal ϕ_{crys} may change as a function of θ_{exp} as explained in Appendix A.

A. Isotropic τ and ω_c

In the presence of a magnetic field a quasiparticle traverses the FS following the contours defined by the dispersion. During this journey the quasiparticle will gain velocity from the electric field until it encounters a scattering event, after which it begins its journey again. As the angle of the field with respect to the crystal axes is adjusted, the quasiparticle will traverse different orbits and the average velocity in the direction of the current can vary dramatically. This picture is formalized in the Chambers' tube integral, which is the solution to the Boltzmann transport equation in the relaxation-time approximation

$$\sigma_{ij} = \frac{e^2}{4\pi^3\hbar^2} \int_{FS} d\mathbf{k} \left(\frac{\partial f_{\mathbf{k}}}{\partial \mathbf{k}} \right) v_i(\mathbf{k}, 0) \int_{-\infty}^0 v_j(\mathbf{k}, t) e^{t/\tau} dt, \quad (4)$$

where $f_{\mathbf{k}}$ is the mean occupation of state \mathbf{k} and τ is assumed to be independent of \mathbf{k} (or equivalently, isotropic in the azimuthal angle ϕ). The Chambers formula can be used in a situation where both closed and open orbits are present.^{33,34} For our particular interest only closed orbits are involved (the FS is q-2D)^{20,25} and we are able to use the simpler Shockley-Chambers tube integral. Furthermore it is easier to use cylindrical coordinates, in line with our description of $k_F(\kappa, \phi)$. The interplane conductivity is then given by

$$\begin{aligned} \sigma_{zz} &= \frac{e^2}{4\pi^3\hbar^2} \int d\varepsilon \left(\frac{-\partial f^0}{\partial \varepsilon} \right) \int d\mathbf{k}_B \\ &\times \int_0^{2\pi} d\phi \frac{v_z(\phi, \mathbf{k}_B, \varepsilon)}{\omega_c} \int_0^\infty d\phi' \frac{v_z(\phi - \phi', \mathbf{k}_B, \varepsilon)}{\omega_c} \\ &\times e^{-\phi/\omega_c\tau}, \end{aligned} \quad (5)$$

where \mathbf{k}_B is the reciprocal space direction parallel to the magnetic field \mathbf{H} , $d\phi = \omega_c dt$ and ω_c is considered isotropic. In order to use Eq. 5 to analyse the ADMR data, we follow Yamaji³⁵ and define a vector k_z^0 as shown in Figure 5(b). The projection of the magnetic field on the azimuthal plane relative to the k_x -axis (corresponding to the Cu-O-Cu bond direction) is labelled ϕ_{crys} (see Figure 5 (a)). Each orbital plane is then defined by three parameters: the polar angle $\theta_{\text{crys}} \equiv \theta$, the azimuthal angle ϕ_{crys} and k_z^0 . The former two are determined during the experiment whereas the latter is an integration variable in the fitting procedure described below.³⁶ The intersection of this plane with the FS gives the path of the quasiparticle in reciprocal space. This plane is given by the equation

$$k_x \sin\theta + k_z \cos\theta = |\mathbf{k}_B| = k_z^0 \cos\theta. \quad (6)$$

This is a convenient notation because k_z can be uniquely described in terms of k_z^0 and the projection of the Fermi wave-vector onto the azimuthal plane as the quasiparticle traverses an orbit, $\mathbf{k}_F^\parallel(\phi)$. In summary

$$k_z = |\mathbf{k}_B| = k_z^0 - k_F^\parallel(\phi) \cos(\phi - \phi_{\text{crys}}) \tan\theta. \quad (7)$$

We make the replacement $\varepsilon \rightarrow \varepsilon_F$ in Eq. 5 by approximating $\partial f^0/\partial \varepsilon \rightarrow \delta(\varepsilon - \varepsilon_F)$ for $kT \ll \varepsilon_F$. The periodicity of $v_z(\phi)$ and $v_z(\phi - \phi')$ in ϕ and $\phi - \phi'$ respectively is of some computational benefit. Taking the Fourier transform of v_z ^{37,38} and writing it as a Fourier sum gives

$$\begin{aligned} v_z(\phi) &= a_0 + \sum_0^\infty a_n \cos n\phi + b_n \sin n\phi, \\ v_z(\phi - \phi') &= c_0 + \sum_0^\infty c_n \cos n(\phi - \phi') + d_n \sin n(\phi - \phi'), \end{aligned} \quad (8)$$

where a_n, b_n, c_n and d_n are Fourier coefficients. Using a Laplace transform and after a few algebraic manipulations, the conductivity is finally given by^{37,38}

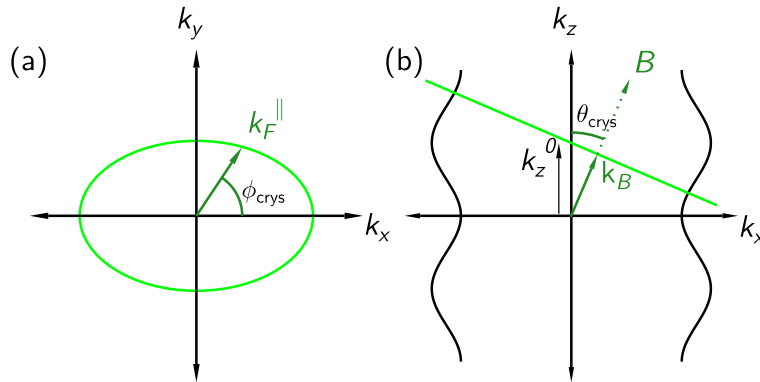


FIG. 5: (Color online) Schematic representation of a single quasiparticle orbit with an oriented magnetic field. Panel (a) gives the projected view of the Fermi surface, defining the azimuthal angle ϕ_{crys} , while panel (b) gives the definition of the parameters k_B , k_z^0 and θ_{crys} .

$$\sigma_{zz} = \frac{e^3 \tau_0 B \cos(\theta)}{2\pi^2 \hbar^2} \int dk_z^0 \omega_0^{-1} \times \left[a_0 c_0 + \frac{1}{2} \sum_{n=1}^{\infty} \left\{ \frac{a_n c_n + b_n d_n}{1 + (\omega_0 \tau_0)^2} - \frac{(a_n d_n - b_n c_n) \omega_0 \tau_0 n}{1 + (\omega_0 \tau_0)^2} \right\} \right], \quad (9)$$

where $\omega_c = \omega_0$ and $\tau = \tau_0$ to emphasize that these parameters are isotropic. Eq. 9 is used to calculate the resistivity in the transverse direction ρ_{zz} by taking the inverse of σ_{zz} , which is correct to a good approximation due to the large anisotropy of the in-plane and interplane resistivity. Because parameters such as the effective mass m^* are not well known, it is usual practice to simulate the relative change in magnetoresistivity $\Delta\rho_{zz}/\rho_{zz0}$, where ρ_{zz0} is the interplane resistivity at zero field, rather than ρ_{zz} directly. This normalization procedure means that the warping parameters in the k_z direction can only be determined as *ratios*. In other words, the ADMR can be used to obtain values for k_{61}/k_{21} and k_{101}/k_{21} but not k_{21} , k_{61} or k_{101} directly.

The parameters we wish to determine therefore are k_{00} , k_{04} , k_{61}/k_{21} , k_{101}/k_{21} and $\omega_0 \tau_0$ (the cyclotron frequency and the scattering time always appear as a product in the sum of Eq. 9 and thus behave as a single parameter). In a number of earlier studies on different Tl2201 crystals, in which all parameters were allowed to vary, a consistent set of FS parameters were obtained.^{15,20,22} This enables us to refine our parameterization and minimize the number of free parameters without losing confidence in their relative magnitudes. We fix k_{00} for example by first obtaining the doping level p using the universal phenomenological relation³⁹ between p and the critical temperature T_c

$$\frac{T_c(p)}{T_c^{\text{max}}} \approx 1 - 82.6(p - 0.16)^2, \quad (10)$$

then adopting the simple hole-counting procedure,

$$(\pi k_{00}^2)/(2\pi/a)^2 = (1+p)/2. \quad (11)$$

Our next simplifying assumption is that $t_{\perp}(\phi)$ vanishes at eight symmetry points on the FS (see Figure 3) as expected from band structure calculations²⁴ and revealed by earlier ADMR measurements.²⁰ For this to be the case, we require

$$1 - \frac{k_{61}}{k_{21}} + \frac{k_{101}}{k_{21}} = 0, \quad (12)$$

which fixes k_{101}/k_{21} to whatever value k_{61}/k_{21} is given. Hence, only three parameters k_{04} , k_{61}/k_{21} and the product $\omega_0 \tau_0$, are used to fit *simultaneously* five polar angle sweeps at different azimuthal angles (in other words, the data are treated as a single data set, not five separate curves). It is important to realize that these constraints could be relaxed without a significant effect on the other key parameters.

The fitting procedure begins by evaluating σ_{zz} for a given polar angle θ_{crys} and azimuthal angle ϕ_{crys} . The c -axis velocity is evaluated $v_z = \hbar^{-1} \partial \varepsilon(\mathbf{k}) / \partial k_z$ as a function of ϕ for a given k_z^0 , where ε is defined by Eq. 3. The k_z dependence is determined by Eq. 7 and substituted into v_z . For the given k_z^0 , the Fourier transform is taken and the sum in Eq. 9 is evaluated. This is then integrated over k_z^0 across the whole Brillouin zone and the result inverted to give $\rho_{zz}(\theta_{\text{crys}}, \phi_{\text{crys}})$. This is calculated for all θ_{crys} and ϕ_{crys} in a single data set. This process is repeated for different parameter values until a best fit is achieved using standard minimization procedures.

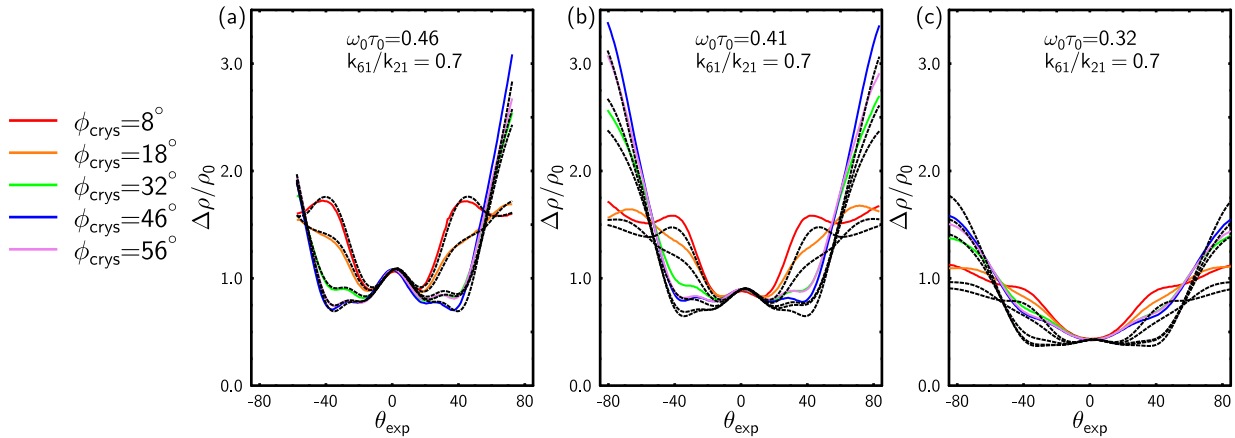


FIG. 6: (Color online) The solid lines are c -axis magnetoresistivity data $\Delta\rho_{zz} = \rho_{zz}(H) - \rho_{zz0}$, normalized to the zero field resistivity ρ_{zz0} , taken at different azimuthal rotations ($\phi_{\text{crys}} = 8^\circ$ (red), $\phi_{\text{crys}} = 18^\circ$ (orange), $\phi_{\text{crys}} = 32^\circ$ (green), $\phi_{\text{crys}} = 46^\circ$ (blue), $\phi_{\text{crys}} = 56^\circ$ (violet) relative to the Cu-O-Cu bond direction) at three different temperatures (a) 4.2 K, (b) 14 K and (c) 50 K. The azimuthal angles given here strictly apply only to $\theta_{\text{exp}} = \pm 90$ due to misalignment of the crystal with respect to the platform axes (see Appendix A for details). The black dashed lines are the best least-squares fits obtained assuming that $\omega_c\tau$ ($= \omega_0\tau_0$) is independent of ϕ and that the parameters k_{04} and k_{61}/k_{21} are fixed to their values at $T = 4.2\text{K}$. Thus only $\omega_0\tau_0$ is allowed to vary with temperature.

The solid lines in Figure 6(a) are ADMR data taken at $T = 4.2\text{K}$ and $\mu_0H = 45$ Tesla, normalized to the zero field resistivity value ρ_{zz0} . Each color represents a different azimuthal angle at which the individual polar ADMR sweeps were taken. Despite the fact that $\omega_0\tau_0$ is less than 0.5 in this sample, the variations in the c -axis magnetoresistance are significant, both with azimuthal and polar angle, thus tightly constraining our parameterization. Note that these data were obtained on a different crystal to those reported in Refs.^{20,22} though the resulting parameterization ($k_{00} = 0.729\text{\AA}^{-1}$, $k_{04} = -0.022\text{\AA}^{-1}$, $k_{61}/k_{21} = 0.7$) is very similar. The best least-squares fits to Eq. 9 are shown as black dashed lines and appear quite adequate for the full range of azimuthal and polar angles studied. (Data at larger angles were not taken at this temperature in order to avoid the large torque forces that accompany a transition to the superconducting state, which occurs here when $H_{c2}(\theta)$ surpasses 45 T.)

Corresponding data and fits for $T = 14\text{K}$ and $T = 50\text{K}$ are shown in panels (b) and (c) respectively. For the fits at higher temperatures (where a larger angular range can be swept), all FS parameters are fixed to their 4.2 K values and only the product $\omega_0\tau_0$ is allowed to vary. The fits rapidly deteriorate as the temperature is raised and are clearly no longer a reliable representation of the data. In fact, even if we allow k_{00}, k_{04} and k_{61}/k_{21} to vary with temperature, the fits do not significantly improve. Furthermore, if k_{00} is allowed to be a free parameter, the fitting procedure tends to minimize at values where the Fermi surface is larger than the first Brillouin zone,

which is clearly unphysical. In response to this failing, we abandon our naive picture of isotropic ω_c and τ and proceed to incorporate anisotropy into the formalism.

B. Isotropic τ and anisotropic ω_c

To illustrate how significant anisotropy in ω_c can be, we consider first the most elementary tight-binding description of an isotropic square 2D lattice. The dispersion of such a system can be described by the equation

$$\varepsilon(\mathbf{k}) - \varepsilon_0 = -2t[\cos(k_x a) + \cos(k_y a)], \quad (13)$$

where $\varepsilon - \varepsilon_0$ describes the quasiparticle dispersion taken relative to some reference (for example, the non-bonding energy ε_0). Quasiparticles complete orbits with a frequency ω_c that depends on the scalar product $\mathbf{k}_F \cdot \mathbf{v}_F$ via the expression

$$\omega_c(\phi, \theta) = eB \cos\theta \frac{\mathbf{k}_F(\phi) \cdot \mathbf{v}_F(\phi)}{\hbar k_F(\phi)^2}. \quad (14)$$

Near the bottom of the band, the quasiparticle orbits in a magnetic field appear almost circular and \mathbf{v}_F is isotropic and nearly parallel to the crystal momentum \mathbf{k} . As ε_F approaches the van Hove singularity (vHs) however, anisotropy in \mathbf{v}_F becomes significant³³ and ω_c develops four-fold anisotropy that essentially becomes infinite at the vHs.

Let us now turn to consider the analogous situation in Tl2201. According to recent ARPES experiments,²⁵ the FS can be fitted by a tight-binding dispersion relation

$$\begin{aligned} \varepsilon - \varepsilon_0 = & \frac{t_1}{2}(\cos k_x + \cos k_y) + t_2(\cos k_x \cos k_y) \\ & + \frac{t_3}{2}(\cos 2k_x + \cos 2k_y) + \frac{t_4}{2}(\cos 2k_x \cos k_y + \cos 2k_y \cos k_x) \\ & + t_5(\cos 2k_x \cos 2k_y), \end{aligned} \quad (15)$$

with $t_1 = -0.725$, $t_2 = 0.302$, $t_3 = 0.0159$, $t_4 = -0.0805$ and $t_5 = 0.0034$ (eV).

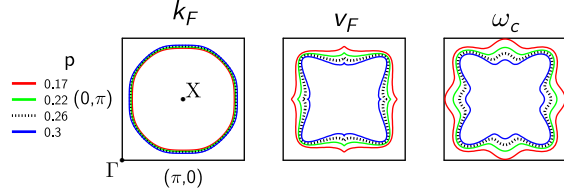


FIG. 7: (Color online) The parameters \mathbf{k}_F , \mathbf{v}_F and ω_c for four different doping levels ($p = 0.17, 0.22, 0.26$ and 0.3) based on the dispersion relation given by Eq. 15 and assuming a rigid band shift. The black dashed line corresponds to the doping level of our $T_c = 17$ K sample.

In order to visualize the doping evolution of the FS parameters according to Eq. 15, we show in Figure 7 the variation of $\mathbf{k}_F(\phi)$, $\mathbf{v}_F(\phi)$ and $\omega_c(\phi)$ (left, center and right panels respectively) for different values of the chemical potential assuming a simple rigid band shift. The energy contours have been centered on the X point of the Brillouin zone. Though the band structure may change with hole doping,⁴⁰ this approximation scheme serves as a good illustration of how the anisotropy in ω_c varies in a comparable way to that in \mathbf{v}_F . As expected, the anisotropy grows as the FS at $(\pi, 0)$ approaches the vHs, though in the doping range relevant to Tl2201, it never exceeds 30%. Interestingly, as the chemical potential is raised, the anisotropy of ω_c changes sign, so that the cyclotron frequency goes from being maximal to being minimal along the zone diagonal, but retaining four-fold symmetry throughout. We approximate this without making any assumptions as to the sign of ω_c using the expression

$$\omega_c(\phi)^{-1} \approx \omega_0^{-1}(1 + \beta \cos(4\phi)). \quad (16)$$

The curves in the right-sided panel of Figure 7 correspond to a range of β values from $\beta \approx 0.3$ (for $p = 0.3$) to $\beta \approx 0$ at optimal doping.

The addition of this extra parameter causes only minor modifications to the fitting procedure. The conductivity is now replaced by the equation

$$\begin{aligned} \sigma_{zz} = & \frac{e^2}{4\pi^3\hbar^2} \int B \cos\theta dk_z^0 \\ & \times \int_0^{2\pi} d\phi \int_0^\infty d\phi' \frac{v_z(\phi, k_z^0, \varepsilon_F)}{\omega_c(\phi)} \frac{v_z(\phi - \phi', k_z^0, \varepsilon_F)}{\omega_c(\phi - \phi')} \\ & \times \exp[h(\phi) - h(\phi - \phi')], \end{aligned} \quad (17)$$

where $h(\phi) = -\int \frac{d\phi}{\omega_c(\phi)\tau_0}$. Under isotropic circumstances $h(\phi) = -\phi/\omega_0\tau_0$ as in Eq. 5. However, in the case where ω_c satisfies Eq. 16, this becomes

$$h(\phi) = -\frac{1}{\omega_0\tau_0} \left\{ \phi + \frac{1}{4}\beta \sin 4\phi \right\}. \quad (18)$$

We can now define two new periodic functions $p_z(\phi)$ and $p_z(\phi - \phi')$ whereby

$$p_z(\varphi) \equiv \frac{v_z(\varphi, k_z^0, \varepsilon_F)}{\omega_c(\varphi)} e^{-\frac{\beta}{4}\sin 4\varphi/\omega_0\tau_0}. \quad (19)$$

The Fourier transform of each function is given by Eq. 8. The form of Eq. 9 is identical, only that ω_0 is interpreted as the average of ω_c within the plane (see Eq. 16). The fitting procedure proceeds as described in Section IV A except our fitted parameters are now $k_{04}, k_{61}/k_{21}, \beta$ and $\omega_0\tau_0$. As before, $k_{00} = 0.729 \text{ \AA}^{-1}$, $k_{04} = -0.022 \text{ \AA}^{-1}$, k_{61}/k_{21} is fixed at low T (4.2 K) and only $\omega_0\tau_0$ and β are allowed to vary as a function of temperature. Figure 8 (a)-(c) shows the best least-squares fits of the same ADMR data under this new parameterization scheme. While the fits are closer to the real data than in the corresponding isotropic case, there is still a clear problem with the higher temperature fits. If we choose to allow k_{61}/k_{21} to vary however, the fits become reasonable at all temperatures, as shown in Figure 8 (d)-(f). The mathematical reason for this is that β has two competing roles: it appears in the exponent $h(\phi)$ and in the ratio $v_z(\phi)/\omega_c(\phi)$. In the latter, β plays a similar role to k_{61}/k_{21} , as can be seen with an expansion using elementary trigonometric identities

$$\begin{aligned} & (\sin 2\phi + \frac{k_{61}}{k_{21}}\sin 6\phi + \frac{k_{101}}{k_{21}}\sin 10\phi)(1 + \beta \cos 4\phi) \\ & = \left(1 - \beta/2 + \frac{\beta k_{61}}{2k_{21}} \right) \sin 2\phi \\ & + \left(\frac{k_{61}}{k_{21}} + \beta/2 + \frac{\beta k_{101}}{2k_{21}} \right) \sin 6\phi \\ & + \left(\frac{k_{101}}{k_{21}} + \frac{\beta k_{61}}{2k_{21}} \right) \sin 10\phi + \frac{\beta k_{101}}{2k_{21}} \sin 14\phi. \end{aligned} \quad (20)$$

The k_{61}/k_{21} , k_{101}/k_{21} and β terms can compensate each other as long as β remains small (that is, so long as

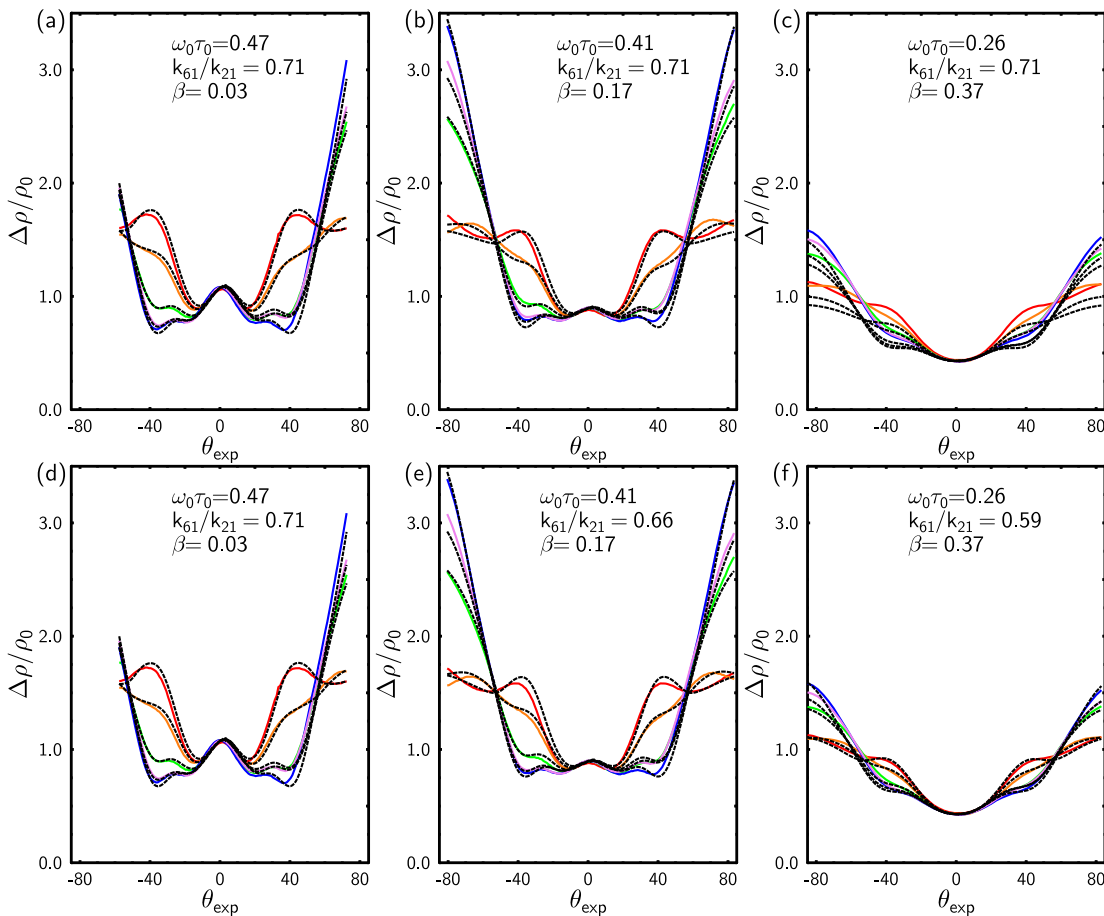


FIG. 8: (Color online) The raw data (solid curves with colors corresponding to ϕ_{crys} as defined in Figure 6) and best least-squares fits (black dashed lines) for ADMR taken at three different temperatures $T = 4.2\text{K}$ (panels (a) and (d)), 14K ((b) and (e)) and 50K ((c) and (f)). In panels (a), (b) and (c), the parameters k_{04} , k_{61}/k_{21} are fixed at their 4.2K values whilst $\omega_0\tau_0$ and β are allowed to vary. In panels (d), (e) and (f), k_{61}/k_{21} is also allowed to vary with temperature.

products such as $\beta k_{101}/2k_{21}$ are negligible). The only non-compensating contribution of β in this expansion is in the multiplication of the $\sin 2\phi$ and $\sin 14\phi$ terms, though perturbations of the former would be noticeable first. In other words, the fitting procedure tends to keep the sum $\beta/2 + k_{61}/k_{21}$ constant as a function of temperature and so the T -dependent changes are contained in the behavior of $h(\phi)$. We return to this point later in our discussion of Figure 10.

The changes in k_{61}/k_{21} and β required to satisfactorily fit the data are significant ($\sim 20\%$ change in k_{61}/k_{21} and a factor of 10 increase in β) and if correct, would imply pronounced FS reconstruction with increasing temperature. Between 4K and 50K , one may expect the Fermi distribution to broaden by around 2% of the band width about the chemical potential. At $p = 0.26$ this is approximately equivalent to a change in nominal doping

of ± 0.02 allowing a change in β of at most ± 0.05 , as is evident from Figure 7. This is significantly less than is required to quantitatively account for the evolution of the ADMR. To our knowledge, the FS restructuring required to fit the present data has never been reported in cuprates and so justifying it would require some very subtle physical arguments. Indeed, photoemission studies have reported insignificant changes as a function of temperature on overdoped compounds.⁴¹ Moreover, in a recent doping dependence study,¹⁵ we found that the overall anisotropy *decreases* with increasing carrier concentration, i.e. as one approaches the vHs, in marked contrast to the band structure picture discussed above and illustrated in Figure 7. In the following section therefore, we turn to consider the effect of anisotropic scattering, which not only allows the data to be fitted accurately but also avoids the physical and mathematical difficulties

we have encountered when considering anisotropy in ω_c alone.

C. Anisotropic τ and anisotropic ω_c

In the most elementary description, the scattering lifetime τ is the average time between collisions of an electron travelling in a metal. In a FL picture however, this is taken to be the mean lifetime of an electron excitation, giving the decay time of a quasiparticle to its ground state near the chemical potential μ . The rate of change of occupation of a state at \mathbf{k} is related to the intrinsic transition rate between two arbitrary states \mathbf{k} and \mathbf{k}' , weighted by the occupation of \mathbf{k} and the lack of occupation of state \mathbf{k}' .

The transition rate cannot be calculated without *a priori* knowledge of the scattering processes that are present. In the limit of elastic scattering however, both \mathbf{k} and \mathbf{k}' are on the same energy surface, and this function is simply $\cos(\phi_{kk'})$, where $\phi_{kk'}$ is the angle between \mathbf{k} and \mathbf{k}' . We then use the relaxation-time approximation, whereby $\mathbb{P}_{\mathbf{k}\mathbf{k}'} = \mathbb{P}(\phi_{kk'})$ is a function of $\phi_{kk'}$ only and this allows a natural definition for the scattering time τ

$$\frac{1}{\tau} \propto \int (1 - \cos(\phi_{kk'})) \mathbb{P}(\phi_{kk'}) \sin(\phi_{kk'}) d\phi_{kk'}. \quad (21)$$

The relaxation time approximation is often an excellent starting point for interpreting transport data and τ is usually considered to be independent of momentum, both of the initial and final state. A more general theory however would allow $\mathbb{P}_{\mathbf{k}\mathbf{k}'}$ to be a function of the initial state \mathbf{k} . In this instance, it may be assumed that the form of Eq. 21 stays very similar,⁴² except that $\mathbb{P}_{\mathbf{k}\mathbf{k}'}$ is now \mathbf{k} -dependent, and hence the replacement $\tau \rightarrow \tau(\mathbf{k})$ needs to be made. In this case, it can be shown⁴² that

$$g_{\mathbf{k}} \Gamma(\mathbf{k}) \equiv \frac{g_{\mathbf{k}}}{\tau(\mathbf{k})} \propto \int \{g_{\mathbf{k}} - g_{\mathbf{k}'}\} \mathbb{P}_{\mathbf{k}\mathbf{k}'} d\mathbf{k}', \quad (22)$$

where $g_{\mathbf{k}} = f_{\mathbf{k}} - f_{\mathbf{k}}^0$, $f_{\mathbf{k}}$ and $f_{\mathbf{k}}^0$ are the probabilities of an electron occupying a state \mathbf{k} in the presence of a field and in equilibrium respectively. $\Gamma(\mathbf{k})$ is the scattering rate. Eq. 22 is general enough to include inelastic scattering mechanisms too (involving energy transfers $\leq k_B T$ for any given scattering event) and this is a direct consequence of the relaxation-time approximation. Such details would normally be contained in $g_{\mathbf{k}}$, and the Boltzmann equation would be very difficult to solve. In the relaxation-time approximation however, these details are deliberately ignored and all that is required for Eq. 22 to hold is that the statistical ensemble of quasiparticles returns to equilibrium between collision events.⁴³

Under these circumstances, we are able to define an anisotropic scattering time that will enter all of our calculations of the conductivity. Since the scattering time

always appears in the product $\omega_c \tau$ in the sum of Eq. 26 it is clear that the procedure for incorporating anisotropic τ will be identical to Section IV B where we introduced anisotropy in ω_c . The simplest model would involve a four-fold anisotropy and in a similar fashion to Sandeman and Schofield¹⁴ or Ioffe and Millis¹¹ we write

$$\Gamma(\phi) = \Gamma_0(1 + \alpha \cos(4\phi)), \quad (23)$$

where $\Gamma_0 \equiv 1/\tau_0$.

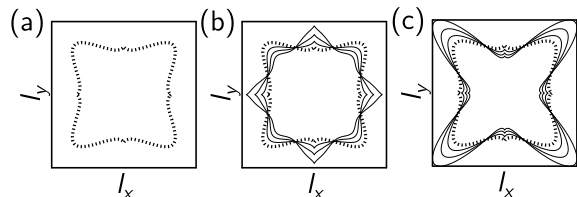


FIG. 9: The mean free path l for three different cases of the anisotropy parameter α for Tl2201 with $p = 0.26$: (a) the isotropic case (dashed) $\alpha = 0$, (b) $\alpha = -0.1, -0.2, -0.3$ (solid, moving inwards along the zone diagonal) and (c) $\alpha = 0.1, 0.2, 0.3$ (solid, moving outwards along (π, π)).

Figure 9 illustrates the effect of this form of scattering rate anisotropy on the mean free path l for the FS derived in Eq. 15 (assuming $p = 0.26$). If $\alpha = 0$, the scattering rate is isotropic and $l(\mathbf{k})$ simply follows the form of $\mathbf{v}_F(\mathbf{k})$ (panel (a)). If $\alpha > 0$ (panel (b)), $\Gamma(\mathbf{k})$ is maximal in the direction parallel to the zone axes and competes with $\mathbf{v}_F(\mathbf{k})$. If, on the other hand, $\alpha < 0$, $\Gamma(\mathbf{k})$ is maximal along the zone diagonals, the anisotropy in $l(\mathbf{k})$ is enhanced in this direction.

With this definition of $\Gamma(\phi)$, the conductivity is identical to Eq. 17 but now we have $h(\phi) = \int \frac{d\phi}{\omega_c(\phi)\tau(\phi)}$ and

$$h(\phi) = -\frac{1}{\omega_0 \tau_0} \left\{ \phi \left(1 + \frac{\alpha\beta}{2} \right) + \frac{1}{4}(\alpha + \beta) \sin 4\phi + \frac{\alpha\beta}{16} \sin 8\phi \right\}, \quad (24)$$

with the periodic functions $p_z(\phi)$ and $p_z(\phi - \phi')$ now redefined as

$$p_z(\varphi) \equiv \frac{v_z(\varphi, k_z^0, \varepsilon_F)}{\omega_c(\phi)} e^{-\frac{(\alpha+\beta)\sin 4\varphi + \frac{\alpha\beta}{16}\sin 8\varphi}{\omega_0 \tau_0}}. \quad (25)$$

The conductivity is then given by

$$\begin{aligned} \sigma_{zz} &= \frac{e^3 \tau_0 B \cos(\theta)}{2\pi^2 \hbar^2} \int dk_z^0 \omega_{\alpha\beta}^{-1} \\ &\times \left[a_0 c_0 + \frac{1}{2} \sum_{n=1}^{\infty} \left\{ \frac{a_n c_n + b_n d_n}{1 + (\omega_{\alpha\beta} \tau_0)^2} - \right. \right. \\ &\left. \left. \frac{(a_n d_n - b_n c_n) \omega_{\alpha\beta} \tau_0 n}{1 + (\omega_{\alpha\beta} \tau_0)^2} \right\} \right], \quad (26) \end{aligned}$$

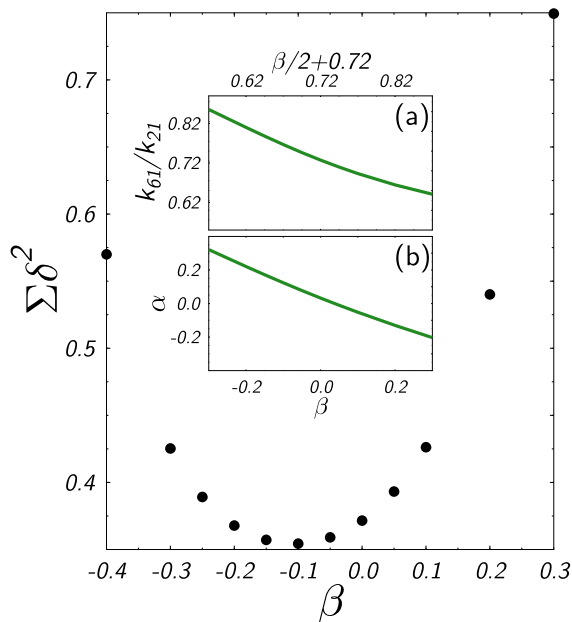


FIG. 10: (Color online) The quality of fit parameterised by the sum $\Sigma\delta^2$ as a function of β , which is given a specific value between -0.4 and 0.3 . Conversely, the parameters $\omega_0\tau_0$, α and k_{61}/k_{21} are free to vary. The parameter $\Sigma\delta^2$ has a broad minimum, indicating that a good fit can be achieved for a broad range of β . Insets (a) and (b) show respectively the interdependence of k_{61}/k_{21} and α on β (see also Eq. 20 and 24). The axes in (a) are shifted as described in the text.

where $\omega_{\alpha\beta} = \omega_0/(1 + \alpha\beta/2)$. Equipped with Eq. 26 we can now follow the procedure described above. The variable parameters are now k_{04} , k_{61}/k_{21} , α , β and $\omega_0\tau_0$. As before we fix k_{00} ($= 0.729 \text{ \AA}^{-1}$) and k_{04} ($= -0.022 \text{ \AA}^{-1}$) and fit the low temperature data with all other parameters free to vary. In this instance however we are now over-parameterized since α and β can compensate each other to within a factor of $\pm\alpha\beta/4$. As a consequence, one cannot accurately quote absolute values for each parameter individually, but rather the *sum* $\alpha + \beta$ (see inset (b) of Figure 10).

We can parameterize the quality of the fits by the sum of squared differences of the data from the fitted curve, which is denoted $\Sigma\delta^2$. As $|\beta|$ becomes large, the terms α and k_{61}/k_{21} are no longer able to compensate and the fits decline in quality. However, as shown in Figure 10, there is also a broad flat region over which $\Sigma\delta^2$ is minimized and one cannot pinpoint the exact value of β . The axes in inset (a) are shifted so that it is apparent that the sum $\beta/2 + k_{61}/k_{21}$ is pinned to a value of about 0.72, a fact which continues to be true at higher temperatures no matter what one forces β to be. Similarly, the value of $\alpha + \beta$ is pinned to nearly zero at low temperature. From

the low- T parameterization used previously to set the FS parameters, we can settle on a value of $\beta \approx -0.1 \pm 0.1$ which is comparable to that estimated from the ARPES-derived dispersion despite being opposite in sign.

Panels (a), (b) and (c) of Figure 11 show the resulting fits to the new parameterization scheme, in which only α and $\omega_0\tau_0$ are allowed to vary with temperature, for $T = 4.2\text{K}$, 14K and 50K respectively. In contrast to previous schemes, the quality of the fits are comparable at all temperatures, without the need for any variation in the other parameters. Hence, by introducing T -dependent anisotropy in the scattering rate, there is no longer any need to invoke FS reconstruction to account for the evolution of the ADMR data. We therefore conclude that this is the most elegant and physically realistic parameterization scheme of all those considered here.

The sign of α is found to be positive, indicating that scattering is weakest along the zone diagonals, as determined previously by azimuthal ADMR measurements.²⁹ As the temperature is raised, α increases markedly. This implies that the anisotropy resides in the *inelastic*, rather than the elastic scattering channel. As with anisotropy in ω_c , anisotropy in the scattering rate can be FS-derived, e.g. due to FS instabilities such as charge-density waves, spin-density waves or antiferromagnetic fluctuations. Spin, charge, or indeed superconducting fluctuations all have specific momentum (and frequency) dependence that is peaked at (or in some cases, confined to) particular regions in \mathbf{k} -space. Anisotropy in τ^{-1} can also signify additional physics due, for example, to strong electron correlations near a Mott insulating state or anisotropic electron-impurity scattering.¹³ The present analysis cannot of course reveal the microscopic mechanism of the anisotropic scattering itself, but can identify some important characteristics of the scattering mechanism, such as its magnitude or its symmetry. Systematic measurements, e.g. as a function of doping and or pressure, would then allow a detailed comparison with the various theoretical proposals and thus help to reveal important hints as to its microscopic origin.

V. CONCLUDING REMARKS

In this paper we have set out a detailed formalism for incorporating in-plane anisotropy, both in the cyclotron frequency and in the transport lifetime, into the analysis of interlayer magnetoresistance of a q2D metal. The focus of the present paper has been to illustrate the need to introduce an anisotropic scattering rate in order to explain the evolution of the ADMR data in overdoped superconducting Tl2201 within a Boltzmann framework. An anisotropic cyclotron frequency $\omega_c(\phi)$ can fit the data, but only if we allow the parameters describing the Fermi surface itself to change as a function of temperature. Given the absence of evidence for such reconstruction, this hypothesis seems unlikely. If, on the other hand, an anisotropic scattering time is introduced, all the FS

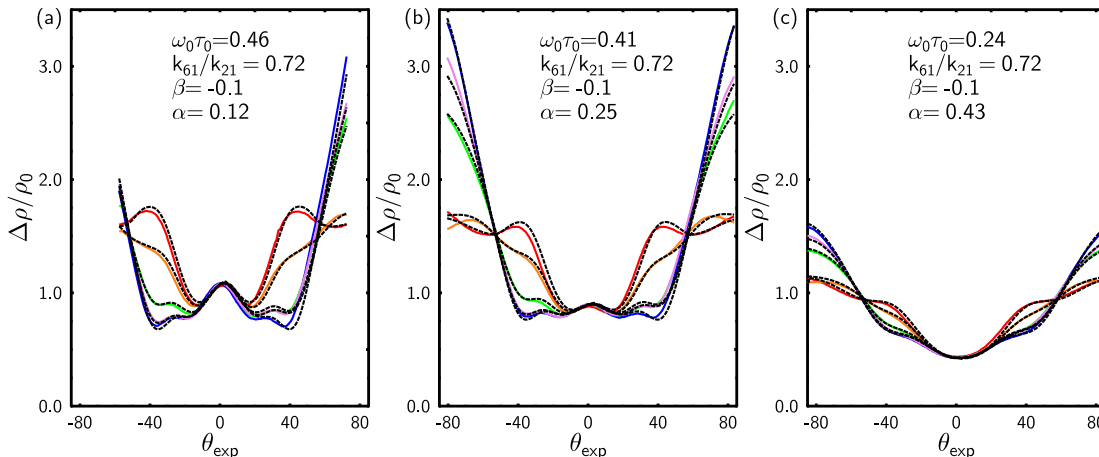


FIG. 11: (Color online) Raw ADMR data (solid curves with colors corresponding to ϕ_{crys} as defined in Figure 6) plotted with the best least-squares fits (black dashed lines) for three different temperatures (a) 4.2 K, (b) 14 K, (c) 50 K. Here both ω_c and τ are considered anisotropic in the azimuthal angle ϕ . The parameters k_{04} , k_{61}/k_{21} and β are fixed to their values determined at $T = 4.2\text{K}$ whilst $\omega_0\tau_0$ and α are allowed to vary as a function of temperature.

parameters can remain constant and *only* $\omega_0\tau_0$ and the anisotropy in $\Gamma(\phi)$ are adjusted. Such a simple parameterization is both elegant and experimentally accurate and we therefore believe it to be the most likely explanation of the observed ADMR data.

A cautionary note is perhaps appropriate here. In the preceding calculations we have assumed the relaxation-time approximation and so the microscopic relaxation dynamics have been ignored. The concept of anisotropic scattering remains valid as long as $\tau(\phi)$ is interpreted as the exponential decay of the distribution between scattering events^{43,44}. However, we cannot rule out more exotic relaxation dynamics that depend on the presence of the magnetic field and hence may be manifested differently if probed by a different means (for example, photoemission). We have discovered that such exotic dynamics do not need to be invoked to explain our ADMR data and conclude that its evolution with temperature, when viewed from a Boltzmann framework using the relaxation-time approximation, is best explained by a scattering rate with a temperature dependent anisotropy.

At high doping levels, lifetime separation in cuprates is less apparent,²⁸ leading some researchers to consider the problem from this perspective. This route has the added advantage of allowing the limits of the conventional Boltzmann transport theory to be explored as one moves across the phase diagram towards to more exotic and potentially non-FL ground state on the underdoped side. The key message here is that by generalizing the theory to include an anisotropic scattering rate $\Gamma(\mathbf{k}) \equiv \tau^{-1}(\mathbf{k})$ one can continue to apply the Boltzmann approach and successfully account not only for the evolution of the ADMR with temperature, but also the dis-

tinct T -dependencies of ρ_{ab} and $\cot\Theta_H$ found in overdoped Tl2201.²² Furthermore, initial measurements of the doping dependence of α in Tl2201 suggest a significant increase in anisotropy in $\tau^{-1}(\mathbf{k})$ as one move towards optimal doping,¹⁵ consistent with the observed increase in lifetime separation (as manifest in the temperature dependence of the Hall coefficient) with decreasing doping.^{5,31,45} The introduction of such anisotropy has proven a fruitful model to understand the normal state of high-temperature superconductors,^{8-12,46-48} though clearly more work is needed to parameterize $\tau^{-1}(\mathbf{k})$ fully and to identify the origin of the anisotropy.

Finally, although the focus of this paper has been a system with body-centered-tetragonal symmetry, the analysis could very easily be generalized to layered systems of other crystallographic symmetries as already pointed out in Ref.²³ and perhaps also one-dimensional systems with anisotropic scattering.⁴⁹ ADMR experiments on BEDT-TTF based organic superconductors have already been performed at low temperature and explained in a Boltzmann framework without the need to invoke an anisotropic scattering rate.³⁴ A full azimuthal and temperature dependence on other salts may however require the introduction of such a parameterization. Similarly the same ideas may also apply to layered charge-density-wave compounds such as the rare-earth tritelurides RTe_3 .⁵⁰ The Boltzmann equation, though simple in its assumptions, thus remains a powerful paradigm whose explanatory power is still to be explored. ADMR is an ideal probe for just such an exploration.

We thank R. H. McKenzie, M. P. Kennett, A. Ardavan and J. A. Wilson for helpful discussions. This work is supported by the EPSRC and a co-operative agreement

between the State of Florida and the NSF. J.A. would like to thank the Lloyd's Tercentenary Foundation.

APPENDIX A: ACCOUNTING FOR SAMPLE MISALIGNMENT IN THE ADMR FITTING PROCEDURE

In this section we illustrate how sample misalignment can be accounted for. The effect of sample misalignment on ADMR has been considered by several authors before this study, in particular Goddard⁵¹ and Abdel-Jawad.³⁷ Before we begin, let us define two frames of reference, that of the laboratory x_p, y_p, z_p , in which the field is parallel to the z_p direction, and that of the crystal x_c, y_c, z_c . The y_p axis is taken as the axis of polar rotation and x_p is perpendicular to this. The normal to the crystallographic plane shall be defined as z_c , and the in-plane directions x_c and y_c shall be taken to be parallel and perpendicular to the copper-oxide bonds respectively. The angle between the field direction and the crystallographic normal z_c gives the crystallographic polar angle θ . The projection of the field onto the $x_c - y_c$ plane gives the crystallographic azimuthal angle ϕ , taken from the x_c axis.

There are two important differences between this study and that of Goddard *et al.*⁵¹ Firstly, instead of correcting experimental θ_{exp} and ϕ_{exp} for misalignment to find the appropriate crystallographic θ and ϕ , we fit the experimental data by including the misalignment in the fitting procedure. Secondly, in the analysis of Goddard,⁵¹ the crystallographic axes x_c and y_c can fall anywhere in the plane of the crystal and do not have assigned direction with respect to the crystal bonds. This gives the misalignment one less parameter, and one of the crystal axes can always fall somewhere in the $x_p - y_p$ plane of the laboratory frame. In the present analysis this is not the case and so three rotations need to be included in the fitting procedure in order to account for every possible misalignment:

- Beginning with the sample aligned with the laboratory frame, there is a misalignment in azimuthal angle denoted by Φ_{asym} , rotated about z_p as shown in Figure 12 (a).
- A rotation about the y_p axis denoted by Θ_{asym}^y as

shown in Figure 12 (b).

- A rotation about the x_p axis denoted by Θ_{asym}^x as shown in Figure 12 (c).

These transformations are elegantly described algebraically. We follow the notation whereby a rotation $R_\beta(\theta)\alpha$ is a rotation of a vector α by angle θ about an axis β . In particular the laboratory axis z_p'' is transformed relative to the crystallographic $z_c(0, 0)$ (before any azimuthal or polar rotation) axis to

$$z_p'' = R_{x_p'}(\Theta_{\text{asym}}^x)R_{y_p'}(\Theta_{\text{asym}}^y)z_c(0, 0), \quad (\text{A1})$$

due to the misalignment of the sample. In an ADMR experiment, the sample is then rotated about the laboratory z_p'' azimuthally by an angle ϕ_{exp} , and then rotated about the x_p'' axis a polar angle θ_{exp} . The position of the crystallographic $z_c(\theta_{\text{exp}}, \phi_{\text{exp}})$ after these azimuthal and polar rotations axis is given by

$$z_c(\theta_{\text{exp}}, \phi_{\text{exp}}) = R_{x_p''}(\theta_{\text{exp}})R_{z_p''}(\phi_{\text{exp}})z_c. \quad (\text{A2})$$

With reference to Figure 13 it is elementary to see that the projection of the field parallel to z_p'' on the crystallographic $z_c(\theta_{\text{exp}}, \phi_{\text{exp}})$ will give θ_{crys} , which should be used to calculate the value of the magnetoresistance in the analysis. Similarly, the projection on the $x_c(\theta_{\text{exp}}, \phi_{\text{exp}}) - y_c(\theta_{\text{crys}}, \phi_{\text{exp}})$ plane will yield ϕ_{crys} . Algebraically we have,

$$\cos(\theta_{\text{crys}}) = z_p'' \cdot z_c(\theta_{\text{exp}}, \phi_{\text{exp}}), \quad (\text{A3})$$

and

$$\tan(\phi_{\text{crys}}) = \frac{z_p'' \cdot x_c(\theta_{\text{exp}}, \phi_{\text{exp}})}{z_p'' \cdot y_c(\theta_{\text{exp}}, \phi_{\text{exp}})}. \quad (\text{A4})$$

The asymmetries for the sample considered in the present paper were estimated to be $\Phi_{\text{asym}} = 8^\circ$, $\Theta_{\text{asym}}^y = 0^\circ$, $\Theta_{\text{asym}}^x = 3^\circ$. The parameter Φ_{asym} was approximately equal to values estimated from diffractometry performed after the ADMR experiment.

¹ For a recent review, see N. E. Hussey in *Handbook on High Temperature Superconductivity: Theory and Experiment* (ed. J. R. Schrieffer and J. S. Brooks, Springer-Verlag, Amsterdam) (2007).

² J. Zaanen *et al.*, Nature Physics **2**, 138 (2006).

³ M. Gurvitch and A. T. Fiory, Phys. Rev. Lett. **59**, 1337 (1987).

⁴ T. R. Chien, Z. Z. Wang and N. P. Ong, Phys. Rev. Lett. **67**, 2088 (1991).

⁵ H. Y. Hwang, B. Batlogg, H. Takagi, H. L. Kao, J. Kwo, R. J. Cava, J. J. Krajewski and W. F. Peck Jr., Phys. Rev. Lett. **72**, 2636 (1994).

⁶ P. W. Anderson, Phys. Rev. Lett. **67**, 2092 (1991).

⁷ C. M. Varma, P. B. Littlewood, S. Schmitt-Rink, E. Abrahams and A. E. Ruckenstein, Phys. Rev. Lett. **63**, 1996 (1989).

⁸ A. Carrington, A. P. Mackenzie, C. T. Lin, and J. R. Cooper, Phys. Rev. Lett. **69**, 2855 (1992).

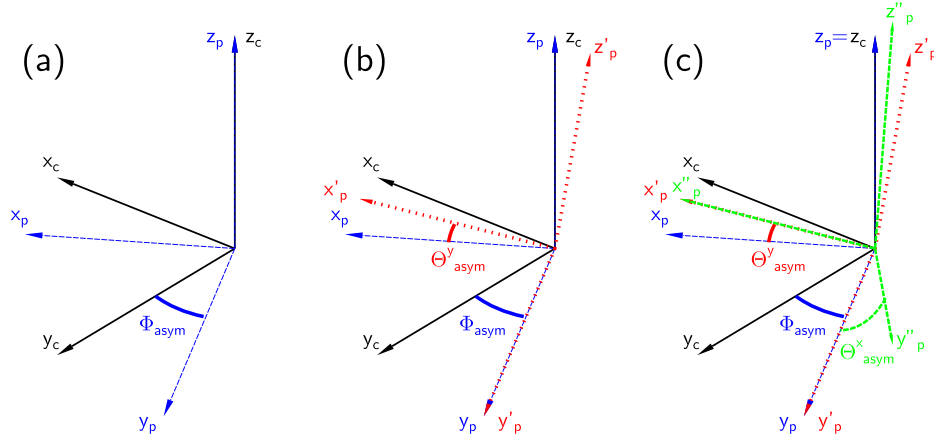


FIG. 12: (Color online) The reference frame of the laboratory x_p, y_p, z_p and that of the crystal x_c, y_c, z_c where x_c is parallel to the copper-oxide bonds. (a) The first misalignment considered is that where the experimental z_p and crystal z_c directions coincide but the axes on the azimuthal plane are offset by an amount Φ_{asym} . The second misalignment considered is that where the experimental and crystal z directions do not coincide. Two rotations are responsible, one about the platform y_p axis by an angle Θ_{asym}^y shown in (b), and another about x'_p by an angle Θ_{asym}^x shown in (c). This gives completely general description of the crystal misalignment with respect to the platform axes.

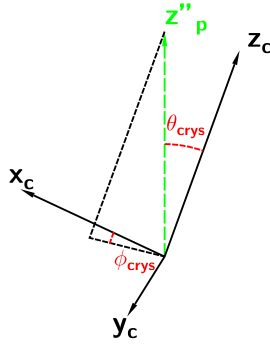


FIG. 13: (Color online) The polar $\theta_{\text{crys}} \equiv \theta$ and azimuthal ϕ_{crys} angles that enter Eq. 17 depend only on the projection of z''_p on the crystal axes. This projection will change as a function of θ_{exp} and ϕ_{exp} and so must be calculated at each point.

⁹ P. Monthoux and D. Pines, Phys. Rev. B **49**, 4261 (1994).
¹⁰ C. Castellani, C. Di Castro and M. Grilli, Phys. Rev. Lett. **75**, 4650 (1995).
¹¹ L. B. Ioffe and A. J. Millis, Phys. Rev. B **58**, 11631 (1998).
¹² N. E. Hussey, Eur. Phys. J. B **31**, 495 (2003).
¹³ C. M. Varma and E. Abrahams, Phys. Rev. Lett. **86**, 4652 (2001).
¹⁴ K. G. Sandeman and A. J. Schofield, Phys. Rev. B **63**, 094510 (2001).
¹⁵ M. Abdel-Jawad, J. G. Analytis, L. Balicas, A. Carrington, J. P. A. Charamant, M. M. J. French, A. P. Mackenzie and N. E. Hussey, Phys. Rev. Lett. (accepted, 2007).
¹⁶ A. A. Kordyuk, S. V. Borisenko, A. Koitzsch, J. Fink, M. Knupfer, B. Behner, H. Berger, G. Margaritondo, C. T. Lin, B. Keimer, S. Ono and Y. Ando, Phys. Rev. Lett. **92**, 257006 (2004).

¹⁷ A. Kaminski, H. M. Fretwell, M. R. Norman, M. Randeria, S. Rosenkranz, U. Chatterjee, J. C. Campuzano, J. Mesot, T. Sato, T. Takahashi, T. Terashima, M. Takano, K. Kadowaki, Z. Z. Li and H. Raffy, Phys. Rev. B **71**, 014517 (2005).
¹⁸ M. V. Kartsovnik, Chem. Rev. **104**, 5737 (2004).
¹⁹ C. Bergemann, A. P. Mackenzie, S. R. Julian, D. Forsythe and E. Ohmichi, Adv. Phys. **52**, 639 (2003).
²⁰ N. E. Hussey, M. Abdel-Jawad, A. Carrington, A. P. Mackenzie and L. Balicas, Nature **425**, 814 (2003).
²¹ L. Balicas, M. Abdel-Jawad, N. E. Hussey, F. C. Chou, and P. A. Lee, Phys. Rev. Lett. **94**, 236402 (2005).
²² M. Abdel-Jawad, M. P. Kennett, L. Balicas, A. Carrington, A. P. Mackenzie, R. H. McKenzie and N. E. Hussey, Nature Physics **2**, 821 (2006).
²³ M. P. Kennett and R. H. McKenzie cond-mat/0610191. Kennett and McKenzie also extended the applicability of this analysis to systems with weakly incoherent interlayer transport.
²⁴ O. K. Andersen, A. I. Liechtenstein, O. Jepsen and F. Paulsen, J. Phys. Chem. Solids **56**, 1573 (1995).
²⁵ M. Platé, J. D. F. Mottershead, I. S. Elfimov, D. C. Peets, R. Liang, D. A. Bonn, W. N. Hardy, S. Chiuzaian, M. Falub, M. Shi, L. Patthey, and A. Damascelli, Phys. Rev. Lett. **95**, 077001 (2005).
²⁶ D. C. Peets, J. D. F. Mottershead, B. Wu, I. S. Elfimov, R. Liang, W. N. Hardy, D. A. Bonn, M. Raudsepp, N. J. C. Ingle and A. Damascelli, New J. Phys. **9**, 28 (2007).
²⁷ N. E. Hussey, A. Carrington, D. C. Sinclair and J. R. Cooper, Phys. Rev. B **50** 13073 (1994).
²⁸ A. P. Mackenzie, S. R. Julian, D. C. Sinclair and C. T. Lin, Phys. Rev. B **53**, 5848 (1996).
²⁹ N. E. Hussey, J. R. Cooper, J. M. Wheatley, I. R. Fisher, A. Carrington, A. P. Mackenzie, C. T. Lin and O. Milat, Phys. Rev. Lett. **76**, 122 (1996).
³⁰ C. Proust, E. Boaknin, R. W. Hill, L. Taillefer and A. P. Mackenzie, Phys. Rev. Lett. **89**, 147003 (2002).
³¹ Y. Kubo, Y. Shimakawa, T. Manako and H. Igarashi, Phys.

- Rev. B **43**, 7875 (1991).
- ³² A. W. Tyler, PhD. thesis, University of Cambridge, 1997.
- ³³ S. J. Blundell, A. Ardavan and J. Singleton, Phys. Rev. B, **55**, R6129 (1997).
- ³⁴ P. A. Goddard, S. J. Blundell, J. Singleton, R. D. McDonald, A. Ardavan, A. Narduzzo, J. A. Schlueter, A. M. Kini and T. Sasaki, Phys. Rev. B **69**, 174509 (2004).
- ³⁵ K. Yamaji, J. Phys. Soc. Japan **58**, 1520 (1989).
- ³⁶ Strictly speaking, ϕ_{crys} and θ_{crys} are equal to ϕ_{exp} and θ_{exp} respectively only when the crystal axes are perfectly aligned with the platform axes. As this is very difficult to achieve, the experiment gives only ϕ_{exp} and θ_{exp} and the angle with respect to the crystal needs to be calculated by fitting the misalignment angles Φ_{asym} , Θ_{asym}^x , Θ_{asym}^y (as described in Appendix A).
- ³⁷ R. Yagi, PhD. thesis, University of Tokyo, Japan, 1991; M. Abdel-Jawad, PhD. thesis, University of Bristol, UK, 2007.
- ³⁸ R. Yagi, Y. Iye, T. Osada and S. Kagoshima, J. Phys. Soc. Japan, **59**, 3069 (1990).
- ³⁹ J. L. Tallon, C. Bernhard, H. Shaked, R. L. Hitterman and J. D. Jorgensen, Phys. Rev. B **51**, 12911 (1995).
- ⁴⁰ G. V. M. Williams, J. L. Tallon, R. Michalak and R. Dupree, Phys. Rev. B **57**, 8696 (1998).
- ⁴¹ C. Kim, F. Ronning, A. Damascelli, D. L. Feng, and Z.-X. Shen, B. O. Wells, Y. J. Kim, R. J. Birgeneau, M. A. Kastner, L. L. Miller, H. Eisaki and S. Uchida, Phys. Rev. B **65**, 174516 (2002).
- ⁴² J. M. Ziman, Phys. Rev. **121**, 1320 (1961).
- ⁴³ R. S. Sorbello, Phys. cond. Matter **19**, 303 (1975).
- ⁴⁴ R. S. Sorbello, J. Phys. F **4**, 505 (1974).
- ⁴⁵ Y. Ando, S. Komiya, K. Segawa, S. Ono and Y. Kurita, Phys. Rev. Lett. **92**, 197001 (2004).
- ⁴⁶ D. van der Marel, Phys. Rev. B **60** R765 (1999).
- ⁴⁷ N. E. Hussey, J. C. Alexander and R. A. Cooper, Phys. Rev. B **74** 214508 (2006).
- ⁴⁸ L. Dell'Anna and W. Metzner, Phys. Rev. Lett. **98**, 136402 (2007).
- ⁴⁹ V. M. Yakovenko and A. T. Zheleznyak, Synth. Met. **103**, 2202 (1999).
- ⁵⁰ J. G. Analytis *et al.*, (unpublished).
- ⁵¹ P. A. Goddard, S. W. Tozer, J. Singleton, A. Ardavan, A. Abate and M. Kurmoo, J. Phys.: Condens. Matter **14**, 7345 (2002).